Figure 18.1. The estimate of excess Gibbs free energy (ΔG) against temperature suggesting a first-order transition. The brown and orange solid lines (indicated as amorphous 1 and 2) represent two extreme estimates of ΔG for the amorphous phase and the dashed lines are extrapolation of these ΔG into the liquid phase. The blue line shows ΔG for the liquid phase and the purple line is the reference crystal phase value. T_{al}, T_{lc}, and T_{ac} (dot-dashed line) represent liquid–amorphous, crystal–liquid, and crystal–amorphous phase transition temperatures, respectively. [Adapted from Donovan et al. [40] with permission.]
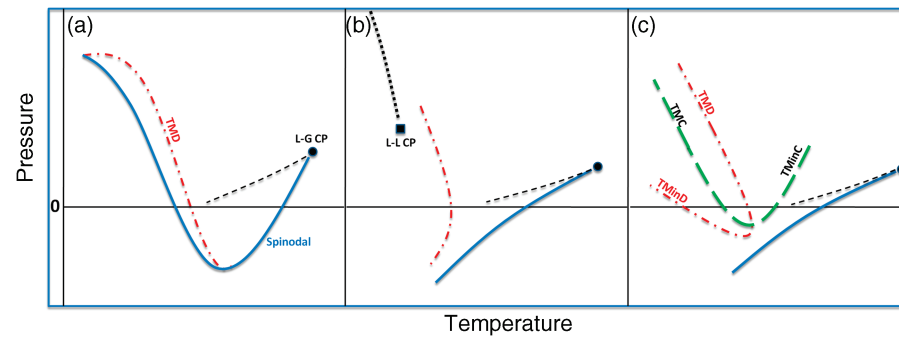
Figure 18.3. Schematic phase diagrams in the pressure–temperature (P, T) plane illustrating three scenarios for liquids displaying anomalous thermodynamic behaviour. (**a**) The spinodal retracing scenario. (**b**) The liquid–liquid critical point scenario. (**c**) The singularity free scenario. The dashed line represent the liquid–gas coexistence line, the dotted line is the liquid–liquid coexistence line, the thick solid line is the liquid spinodal, the long dashed lines is the locus of compressibility extrema and the dot-dashed line is the locus of density extrema. The liquid–gas critical point is represented by filled circle and the liquid–liquid critical point by filled square.
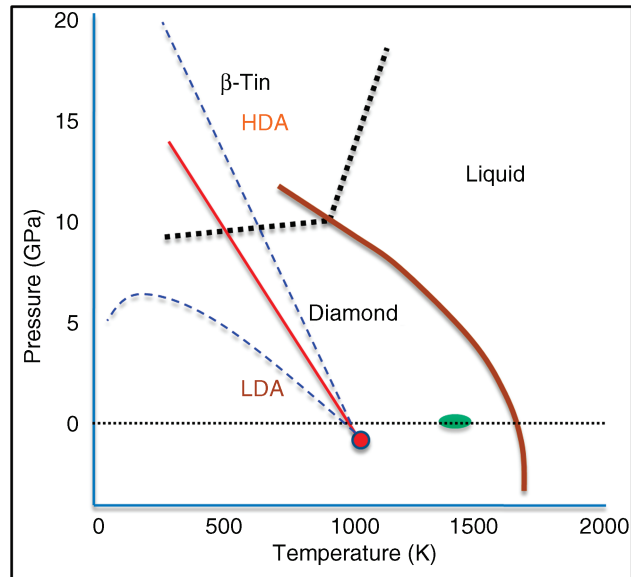
Figure 18.4. Schematic phase diagram of metastable silicon in the pressure–temperature (*P*, *T*) plane discussed in [20,113]. The brown solid line represents the liquid–crystal (cubic diamond) transition line, extended into the *β*-Tin phase. The dotted lines represent the liquid-*β*-Tin and the Cubic diamond-*β*-Tin transition lines. The red line is the liquid–liquid phase transition line ending at a critical point represented by a red circle. The blue lines represent the spinodals associated with the liquid–liquid transition. The green oval symbol represents the amorphous–liquid transition as predicted by some of the earlier experiments. [With permission from McMillan [20,113].]
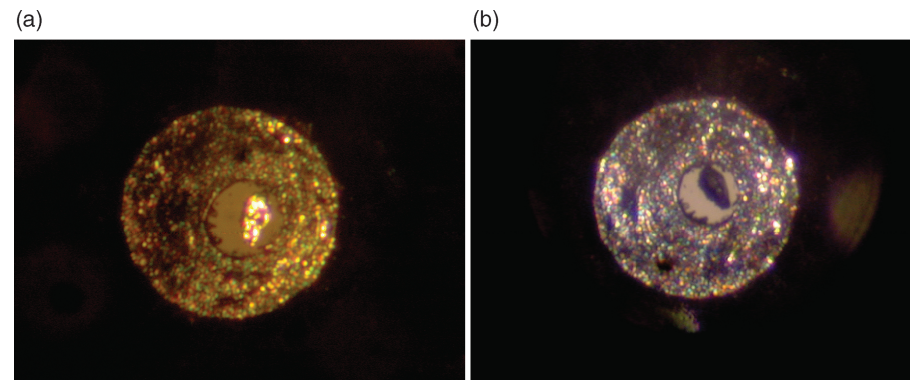
Figure 18.5. Optical micrographs of an amorphous silicon sample show that HDA at $P = 16.6$ GPa (**a**) is highly reflective and LDA at $P = 13.5$ GPa (**b**) is nonreflective (compared to the surrounding metal gasket). [With permission from McMillan and Daisenberger [28,114].]
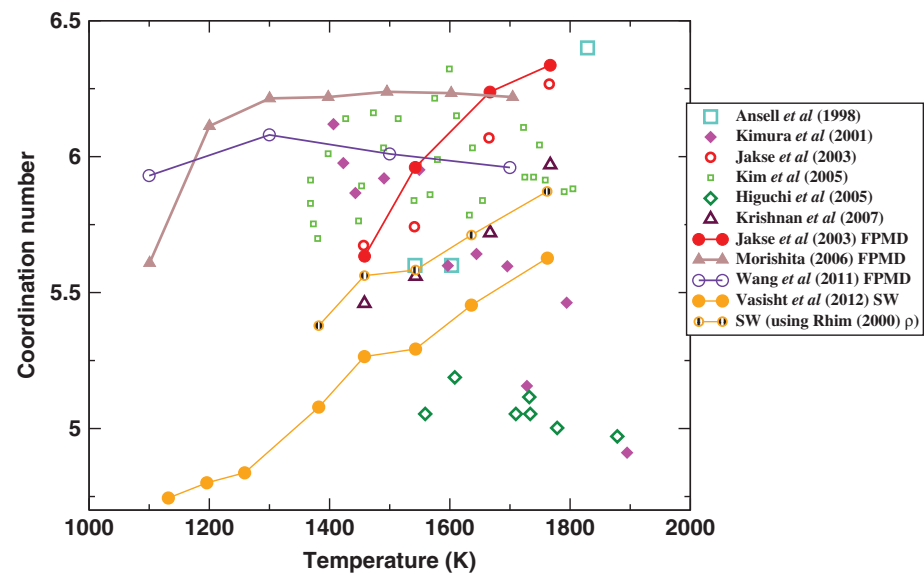
Figure 18.6. Compilation of coordination number measurements plotted against temperature (at $P = 0$ GPa) as reported by different experimental reports, first-principle MD (FPMD) simulations as well as classical simulations results. [From Ansell et al. [73], Kimura et al. [77], Jakse et al. [74], Kim et al. [81], Higuchi et al. [76], Krishnan et al. [75], Morishita [45], Wang et al. [105] with permission.]
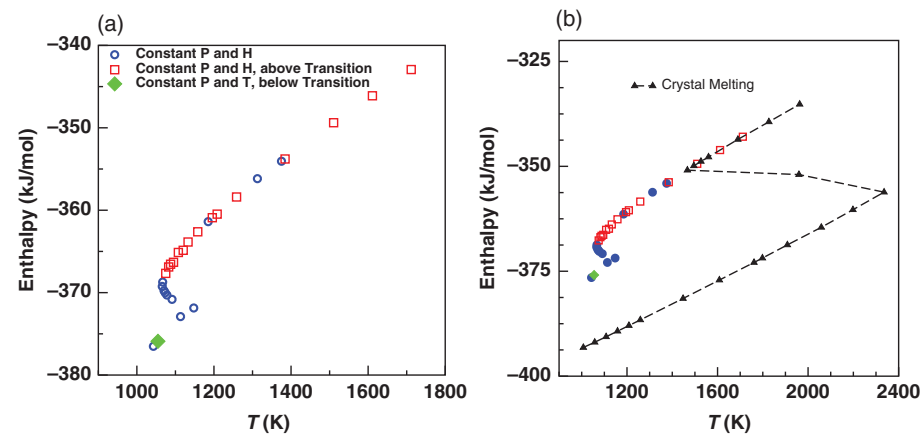
Figure 18.7. (**a**) The enthalpy against temperature from NPH MD simulations and NPT MD simulations using the SW potential for the supercooled liquid above and below the liquid–liquid transition. (**b**) The crystal-liquid transition is shown for comparison with the liquid–liquid transition data. [From Sastry et al. [21] with permission.]
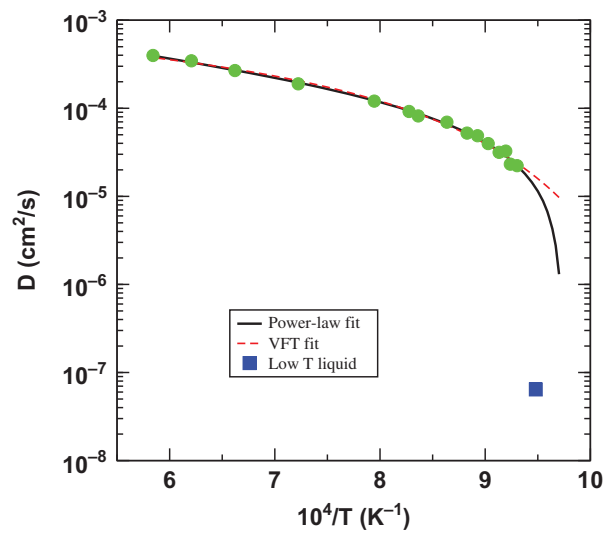
Figure 18.8. The diffusion coefficient D against the inverse temperature, above and below the liquid–liquid transition from MD simulations using the SW potential. In the high-temperature liquid, the diffusivity shows a strongly non-Arrhenius temperature dependence. [From Sastry et al. [21] with permission.]
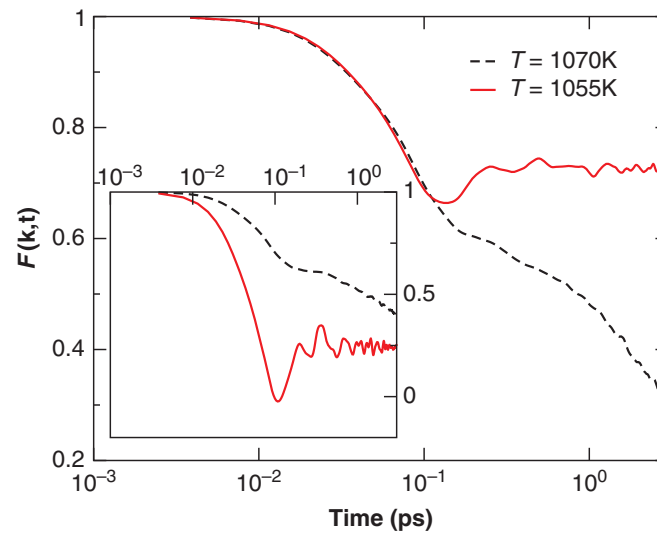
Figure 18.9. *Main panel*: The intermediate scattering function F(k,t) from MD simulations using the SW potential of 512 particles, above and below the transition. The low-temperature liquid displays damped oscillatory behavior, characteristic of strong liquids. The high-temperature liquid shows a monotonic decrease, characteristic of fragile liquids. *Inset*: The intermediate scattering function for smaller system size (108 particles). [From Sastry et al. [21] with permission.]
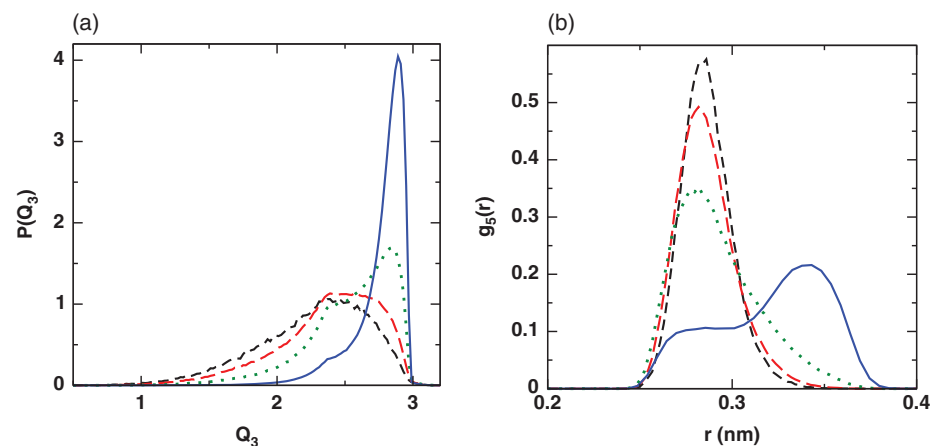
Figure 18.10. (**a**) The distribution of local bond orientation order parameter (Q_3) from MD simulations using the SW potential. The continuous line is for the low-temperature liquid, which indicates local tetra-hedral ordering. (**b**) The fifth neighbour distance distribution $g_5(r)$. For the high temperature liquid (dotted lines), $g_5(r)$ show a uni-modal peak indicating that the fifth neighbour is within the first-coordination shell. For the low-temperature liquid (blue solid line), a bimodal distribution emerges indicating the expulsion of the fifth neighbour in most cases to distances outside the first-coordination shell. [From Sastry et al. [21] with permission.]
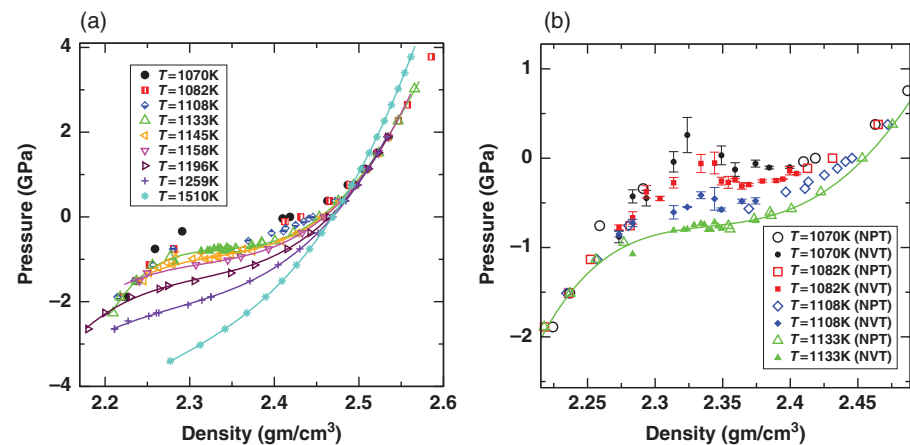
Figure 18.11. Equation of state from NPT MD and NVT MD simulations using the SW potential. Nine isotherms at temperatures above and below the critical temperature of the liquid–liquid transition are shown. The open symbols represent data from NPT MD simulations and the opaque symbols represent data from NVT MD simulation. The solid lines are polynomial fits to the data points. (**a**) The isotherms above $T = 1133$K are monotonic and continuous and below $T = 1133$K show a jump in density for small change in pressure in constant pressure simulations. (**b**) Constant volume (NVT) MD simulation data for $T < 1133$K show nonmonotonic behavior indicating a first-order phase transition.
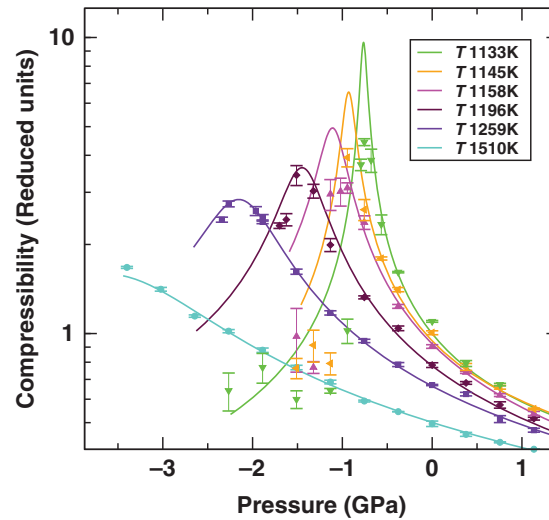
Figure 18.12. Isothermal compressibility against pressure for different temperatures from NPT MD simulations using the SW potential. All the isotherms shown in this figure are for temperatures above the liquid–liquid critical temperature. With the decrease in temperature, the maximum value of the compressibility along an isotherm increases, suggesting an approach to the critical point. The lines represent the compressibility values calculated from the equation of state by numerical differentiation. The symbols represent the compressibility calculated from volume fluctuations.

Figure 18.13. Equation of state of supercooled silicon obtained from first-principles MD (FPMD) simulations displaying a van der Waals-like loop for $T < 1232$K. [From Ganesh et al. [23] with permission.]
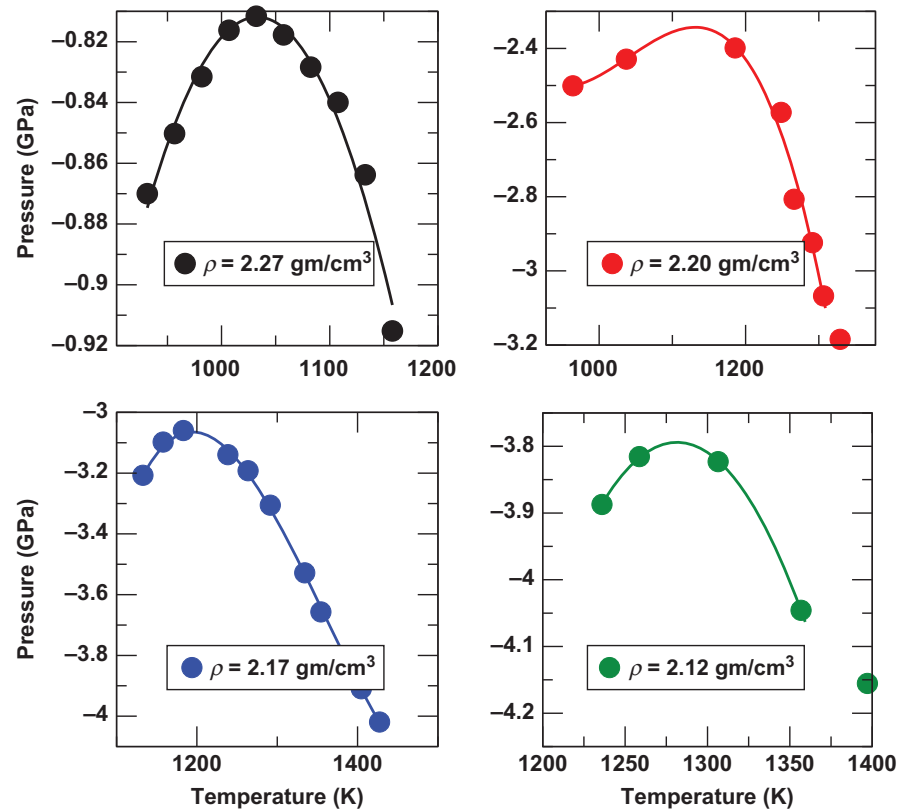
Figure 18.16. Pressure against temperature for different isochors from parallel tempering MC simulations using the SW potential. The location of the maxima along the isochors defines the TMinD line.
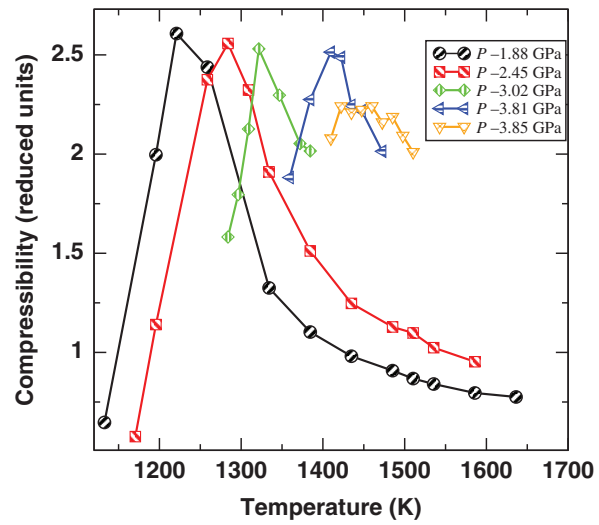
Figure 18.18. Isothermal compressibility against temperature for different isobars from MD simulations using the SW potential. The location of the maxima along the isobars defines the TMC line.
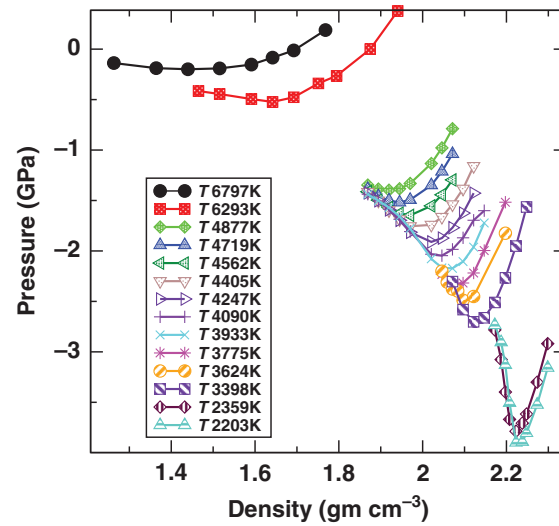
Figure 18.19. Pressure against density for high-temperature isotherms ($T > 2200K$) from NPT MD simulations using the SW potential. The location of the minima along the isotherms defines the spinodal line.
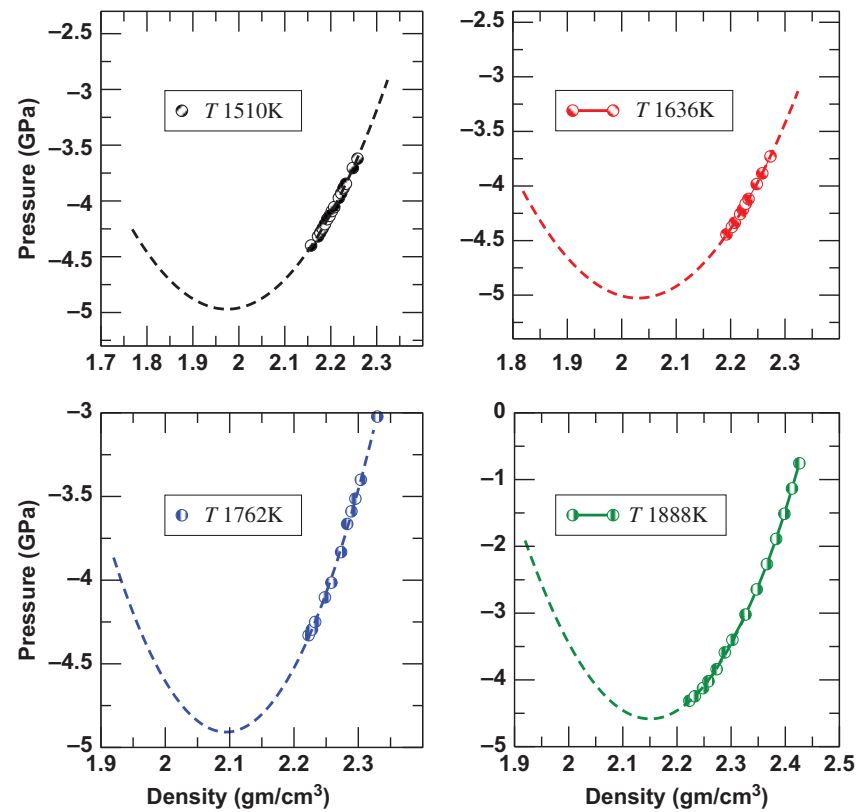
Figure 18.20. Pressure against density for low-temperature isotherms ($T < 2200K$) from MD simulations using the SW potential. The dashed line indicates the quadratic extrapolation of the form $p_0 + a1 \times (\rho - \rho_0) + a2 \times (\rho - \rho_0)^2$ that are used to locate the spinodal.
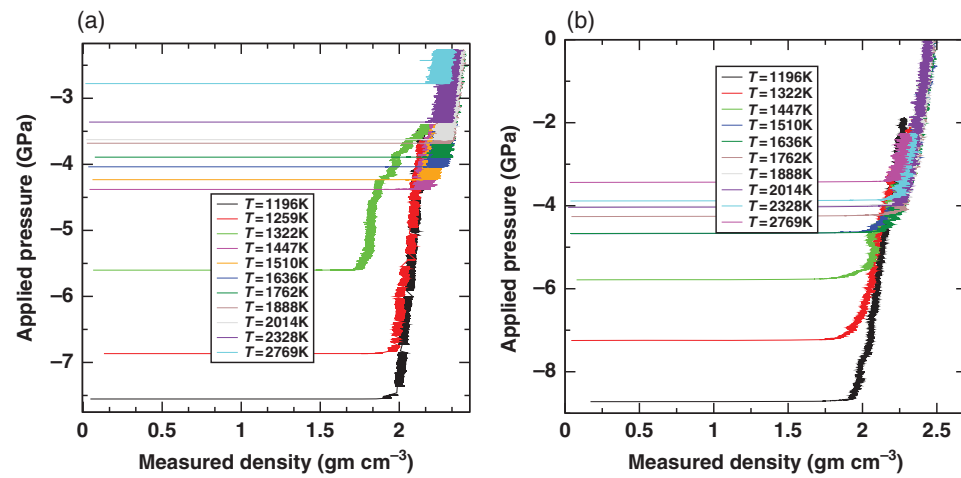
Figure 18.21. Applied pressure against measured density for different temperatures from NPT MD simulations using the SW potential. The stretching rate in (a) corresponds to 0.1 MPa/ps and in (b) corresponds to 10.0 MPa/ps.
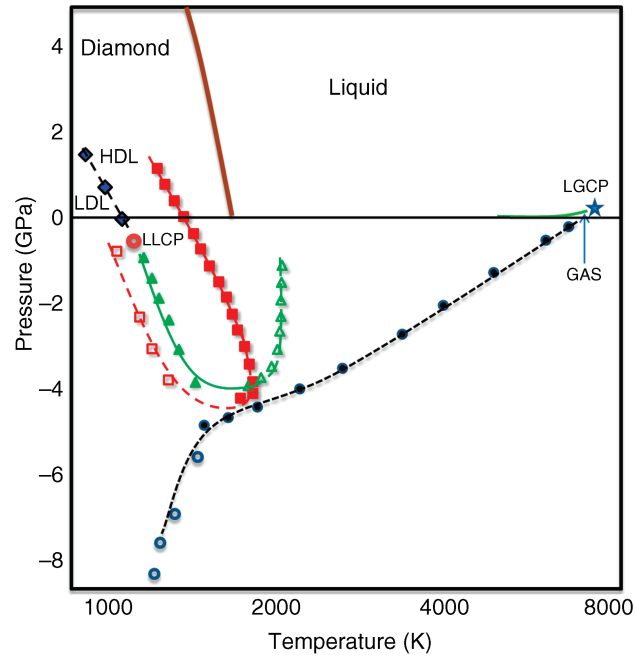
Figure 18.23. The phase diagram of supercooled silicon in pressure–temperature (P, T) plane obtained from simulations using the SW potential. The phase diagram shows the location of (i) the liquid–crystal phase boundary [115]—brown solid line, (ii) the liquid–gas phase boundary and critical point—green line and a star, (iii) the liquid–liquid phase boundary and critical point—filled diamond and a thick circle, (iv) the liquid spinodal—filled circle (v) the tensile limit—open circle (vi) the density maximum (TMD) and minimum (TMinD) lines— filled and open squares, and (vii) the compressibility maximum (TMC) and minimum (TMinC) line—filled and open circle. Lines joining TMD and TMinD (dot-dashed), TMC and TMinC (solid), Spinodal (black dotted line) are guides to the eye.
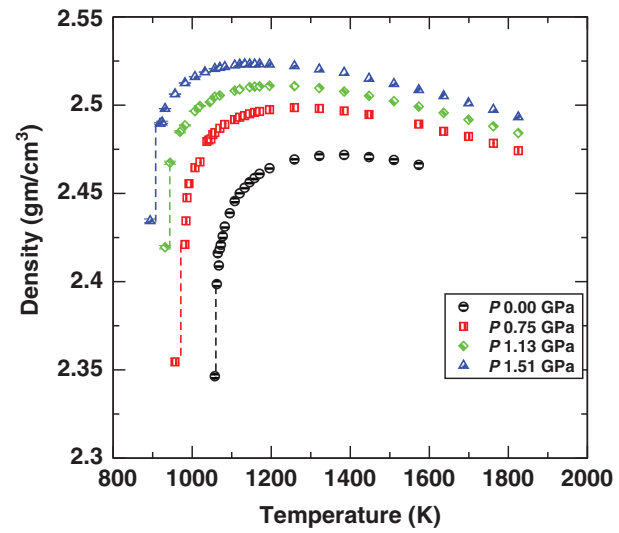
Figure 18.24. Density against temperature for four different isobars from NPT MD simulations using the SW potential. The jumps in the isobars were used to identify the liquid–liquid transition line.
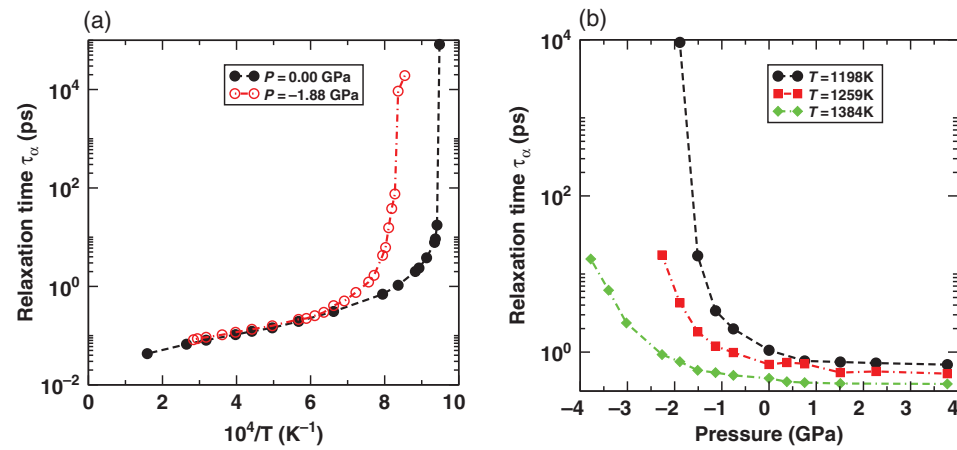
Figure 18.25. (**a**) Relaxation time (τ_α) against inverse temperature at $P = 0$ GPa and $P = -1.88$ GPa from NPT MD simulations using the SW potential. (**b**) Relaxation time against pressure at $T = 1198$K, $T = 1259$K and $T = 1384$K from NPT MD simulations using the SW potential.
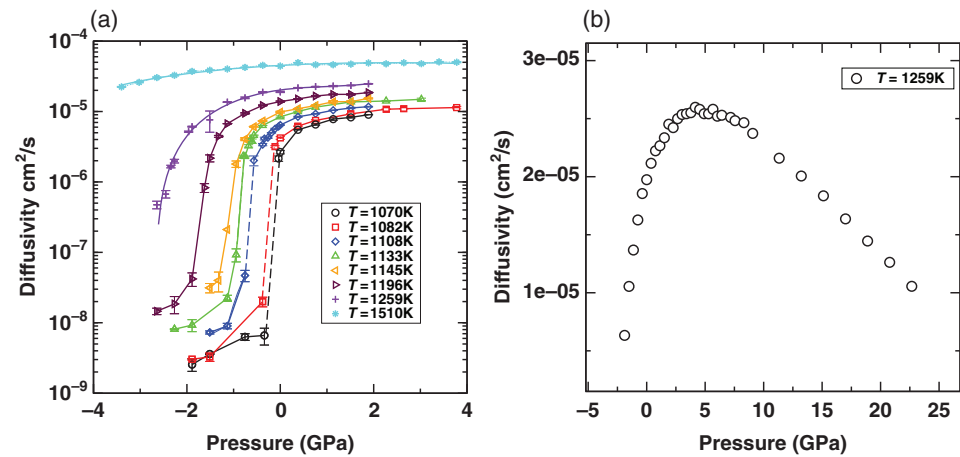
Figure 18.26. Diffusivity against pressure from NPT MD simulations using the SW potential: (a) For different isotherms. Diffusivity decreases with decrease in pressure. (b) For $T = 1259$K. Diffusivity goes through a maximum at around 4.5 GPa.

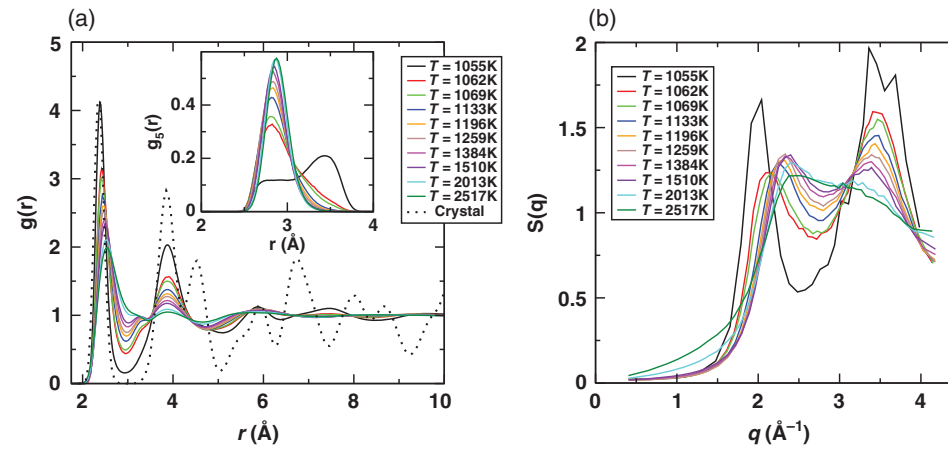**Figure 18.27.** (**a**) The pair correlation function g(r) and (**b**) the structure factor S(q) for different temperatures at $P = 0$ GPa from NPT MD simulations using the SW potential. The inset in (**a**) shows the fifth neighbor distribution.
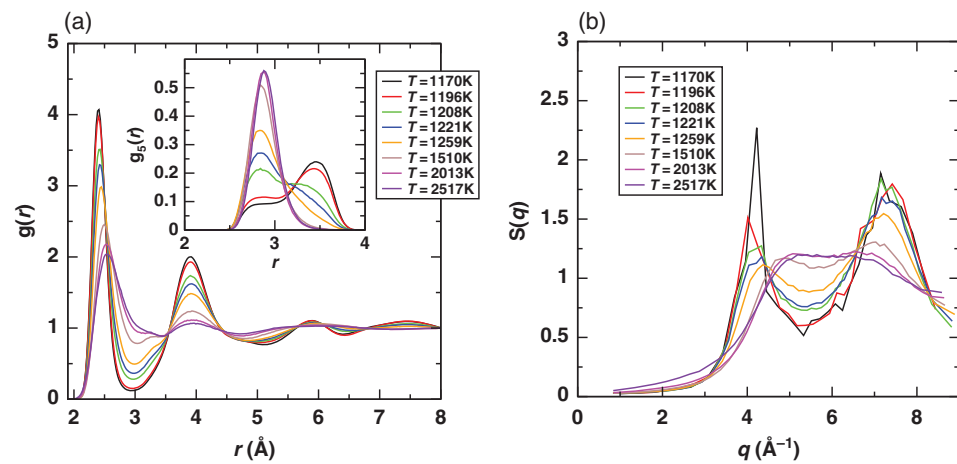
Figure 18.28. (a) The pair correlation function g(r) and (b) the structure factor S(q) for different temperatures at $P = -1.88$ GPa from NPT MD simulations using the SW potential. The inset in (a) shows the fifth neighbor distance distribution.
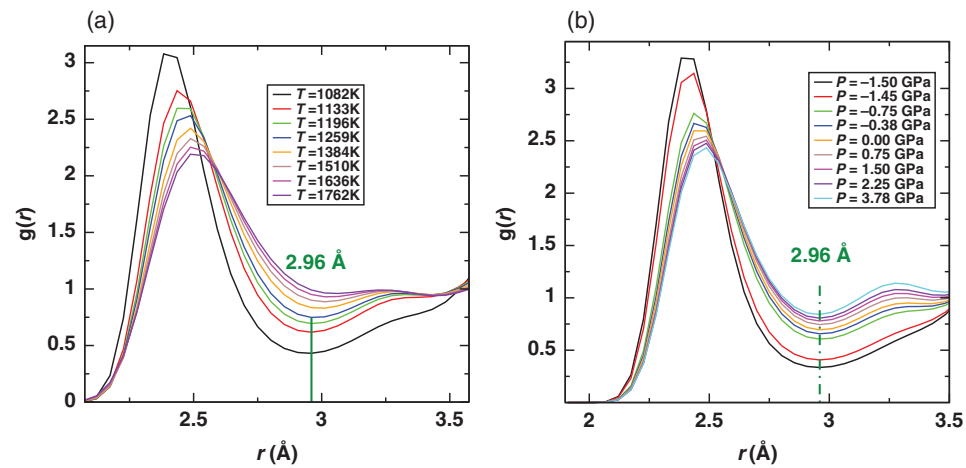
Figure 18.29. The pair correlation function g(r) from NPT MD simulations using the SW potential: (**a**) At different temperatures at $P = 0$ GPa. The first minimum of $g(r)$ remains unchanged till $T < 1259$K. (**b**) At different pressures at $T = 1196$K. The first minimum of $g(r)$ remains fairly unchanged for a wide range of pressure alues.
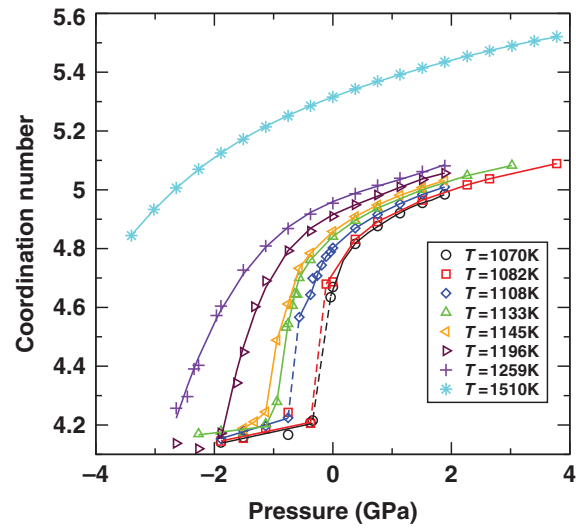
Figure 18.30. Coordination number against pressure at different temperatures from NPT MD simulations using the SW potential. The coordination number for the HDL phase varies from 4.6 to 5.4. In the LDL phase, the coordination number is around 4.2.
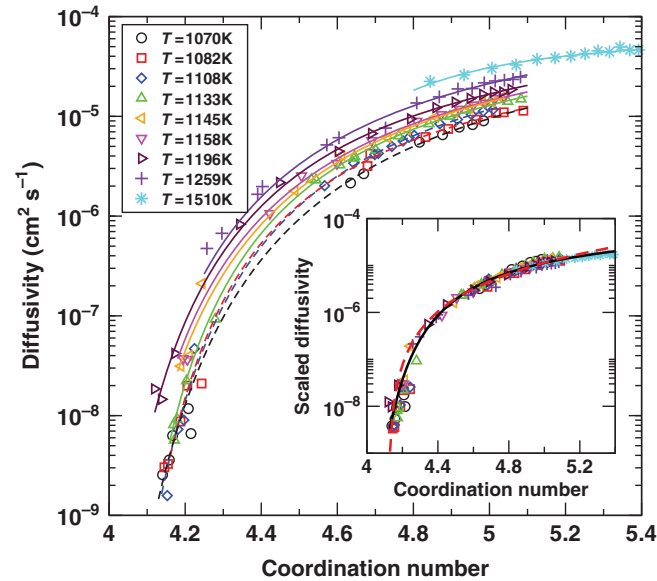
Figure 18.31. Diffusivity (D) against coordination number (C_{nn}) at different temperatures from NPT MD simulations using the SW potential. Lines through the data points are guides to the eye, and highlight the remarkably similar dependence of D on C_{nn} at all temperatures, including those below the critical temperature, where both D and C_{nn} change discontinuously. (*Inset*) Diffusivity (scaled to match at $C_{nn} =$ 4.8) versus C_{nn}, showing data collapse. The solid line is a Vogel–Fulcher–Tammann (VFT) fit, with a C_{nn} of vanishing diffusivity = 3.86. The dashed line is a power law fit, with a coordination number of vanishing diffusivity = 4.06.
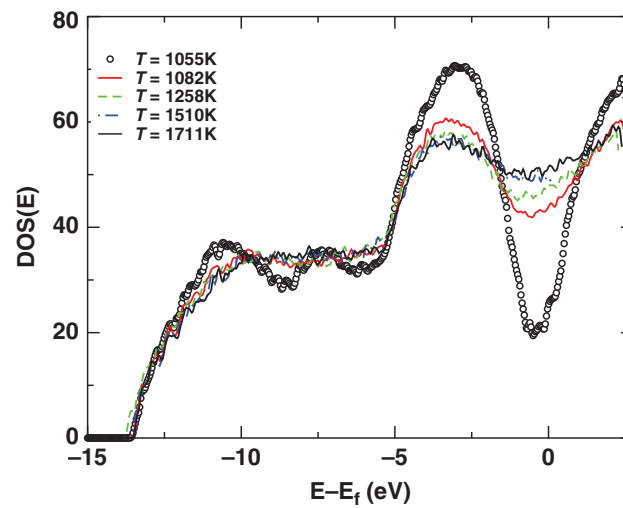
Figure 18.32. Electronic DOS of the LDL at 1055K, HDL at 1082K and high temperature liquid phases from DFT calculations on the MD trajectory obtained using the SW potential. [From Ashwin et al. [26] with permission]
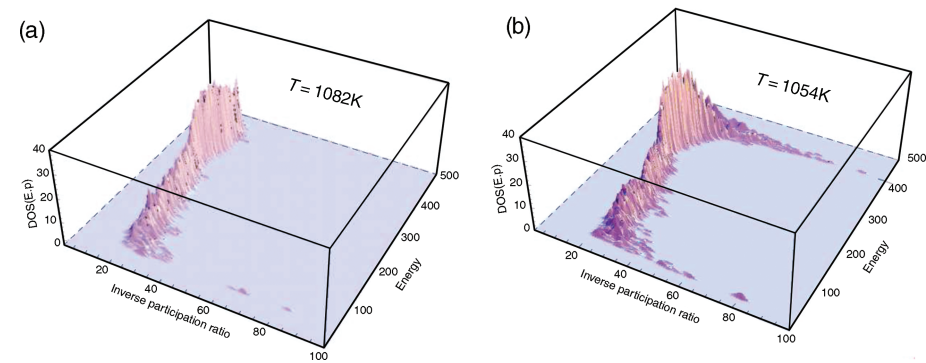
Figure 18.33. Electronic DOS as a function of energy and inverse participation ration for (**a**) $T = 1082$K and (**b**) $T = 1054$K from DFT calculations on the MD trajectory obtained using the SW potential. The states near the Fermi energy at $T = 1054$K are localized. [From Ashwin et al. [26] and SS Ashwin *Ph D* thesis, JNCASR (2005) with permission.]

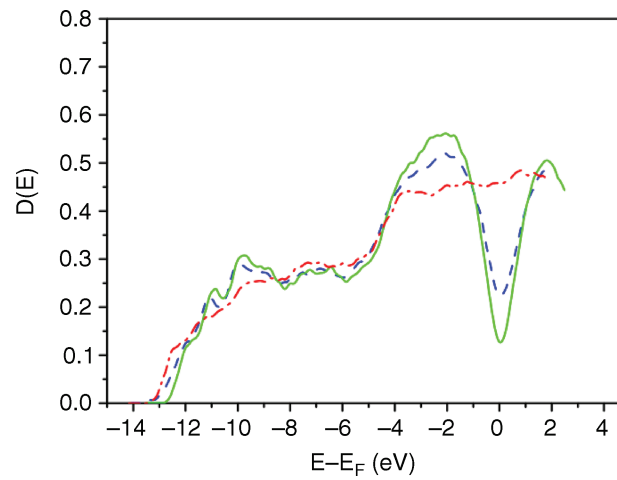**Figure 18.34.** Electronic DOS of the LDL at 1050K(solid line), HDL at 1070K(dashed line) and high T liquid at T_m (dot-dashed line) phases from first-principles MD (FPMD) simulations. [From Jakse et al. [22] with permission.]
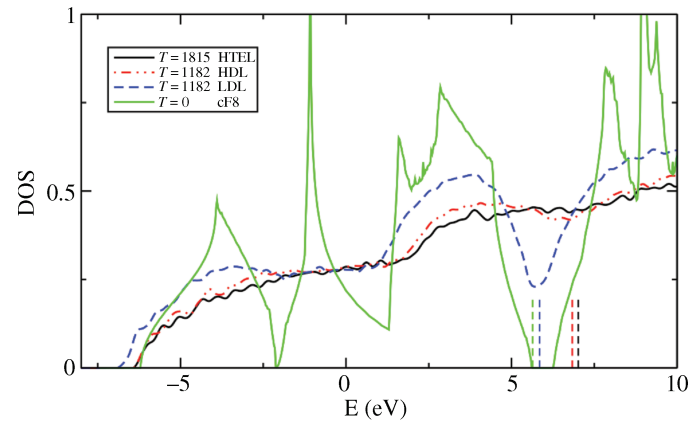
Figure 18.35. The plot of electronic DOS of the crystal (green), LDL (blue), HDL (red) and high T liquid (black) phases from first-principles MD (FPMD) simulations. Fermi energy E_F for each of the phases is represented by vertical dashed lines. [From Ganesh et al. [23] with permission.]
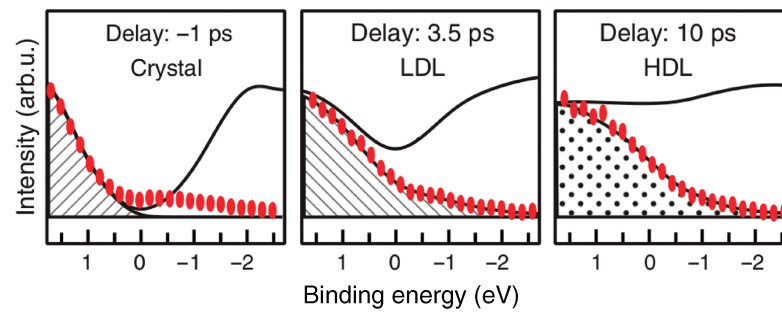
Figure 18.36. Electronic DOS of the crystal, LDL, and HDL phases. Measured data points for the occupied electronic states are represented by red ovals and black lines are from calculations. [From Beye et al. [30] with permission.]
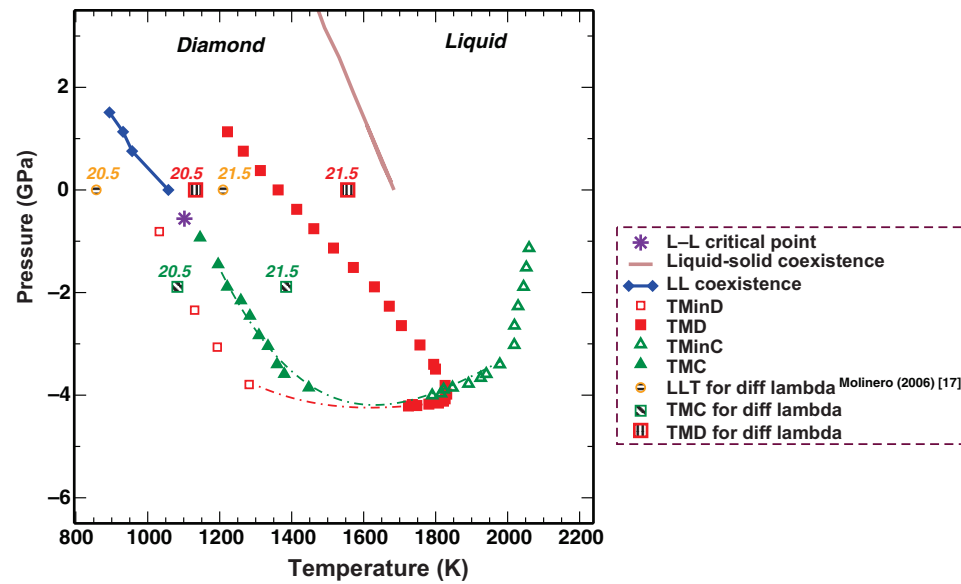
Figure 18.37. Phase diagram of supercooled silicon (in PT plane) at $\lambda = 20.5, 21.0(Si)$ and 21.5 from MD simulations using the SW potential. The liquid–liquid transition points [100] are shown as filled diamonds, the density extrema points are shown as squares and compressibility maxima points are shown triangles. The values of λ are stated over the symbols.
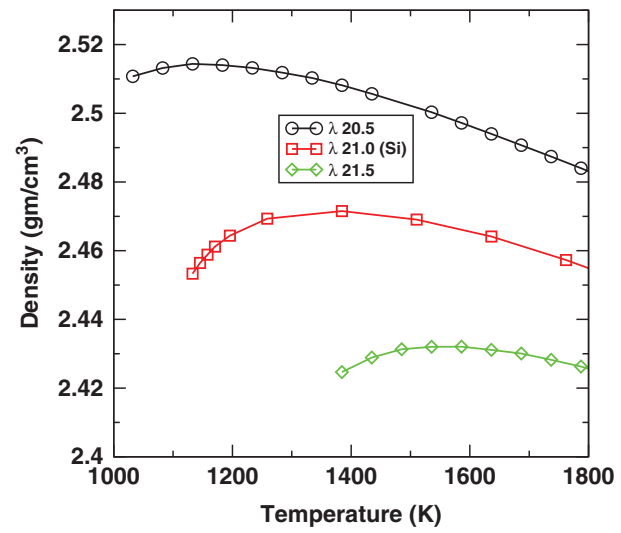
Figure 18.38. Density against temperature for three different values of λ from NPT MD simulations using the SW potential.
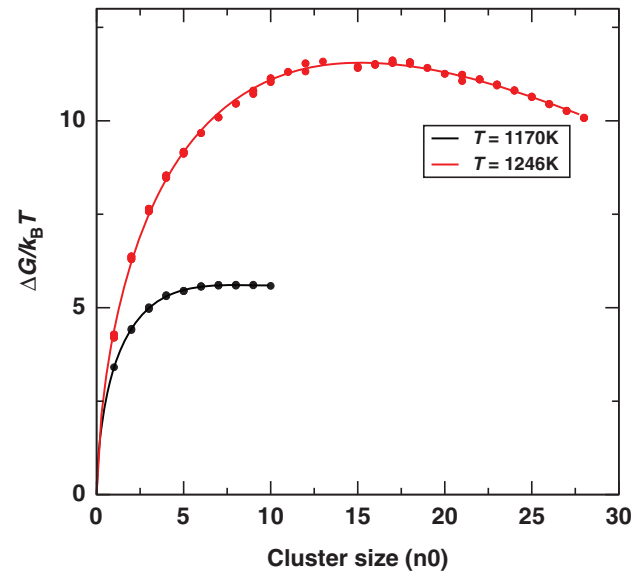
Figure 18.39. The estimate of Gibbs free energy barrier ($\Delta G/k_\mathrm{B}T$) against the largest crystalline cluster size ($n0$) at $P = 0$ GPa from Umbrella Sampling Monte Carlo simulations using the SW potential.
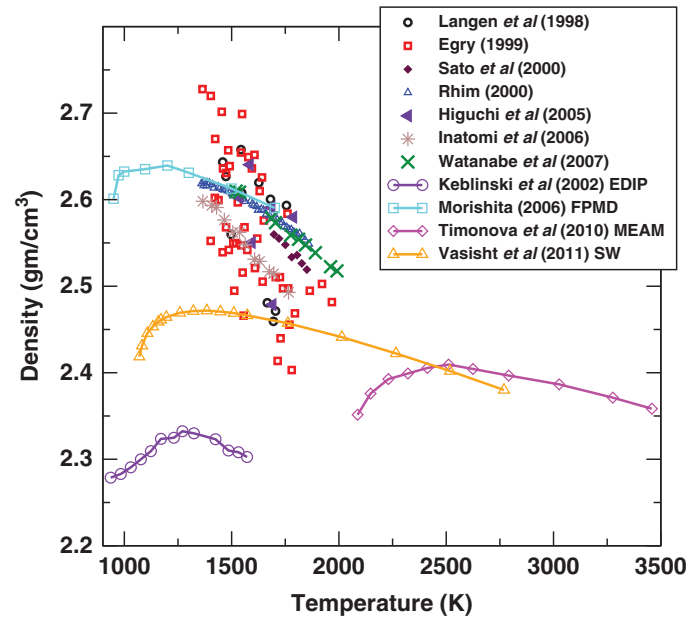
Figure 18.40. Compilation of density against temperature from different experiments and simulations. The experimental data are represented by symbols and the simulation data are represented by line and symbol. [From Langen et al. [82], Egry [79], Sato et al. [83], Rhim [50], Higuchi et al. [76], Inatomi et al. [80] and Watanabe et al. [78], Keblinski et al. [102], Morishita [45] and Timonova et al. [103] with permission.]
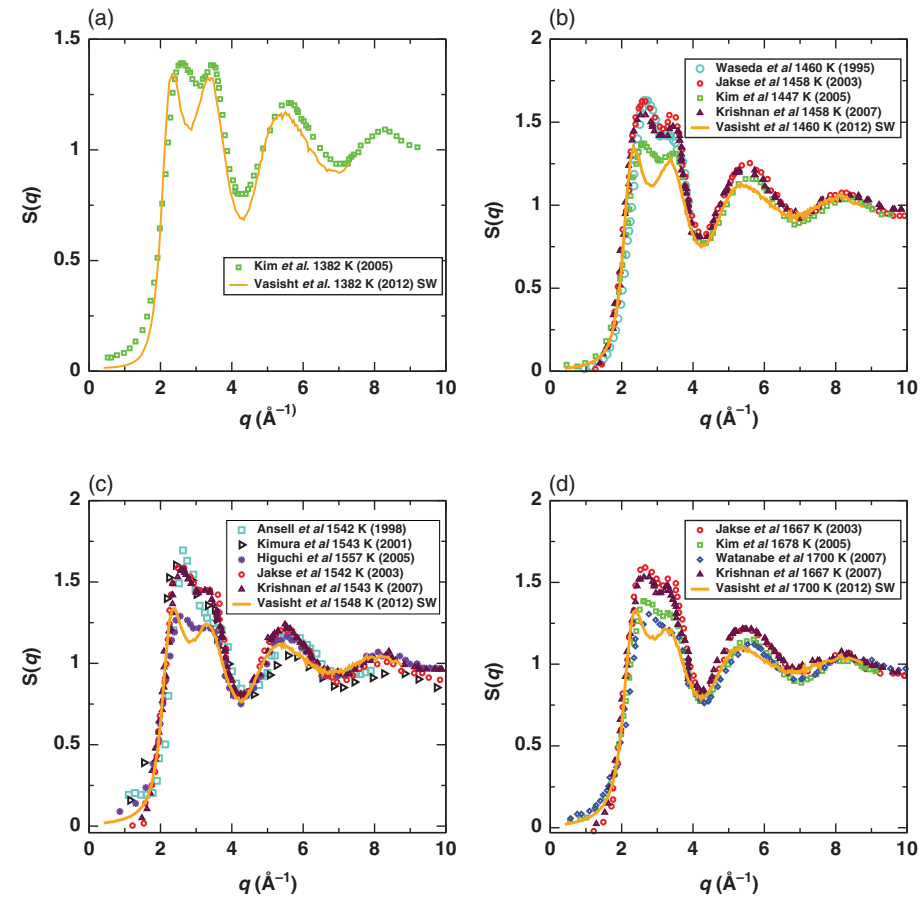
Figure 18.41. Comparison of the structure factor S(q) from NPT MD simulations using the SW potential and from experiments at four different temperatures, $T = 1382K$, $T \approx 1455K$, $T \approx 1550K$ and $T \approx 1770K$. [From Waseda et al. [104], Ansell et al. [73], Kimura et al. [77], Jakse et al. [74], Higuchi et al. [76], Kim et al. [81], Watanabe et al. [78], Krishnan et al. [75] with permission.]
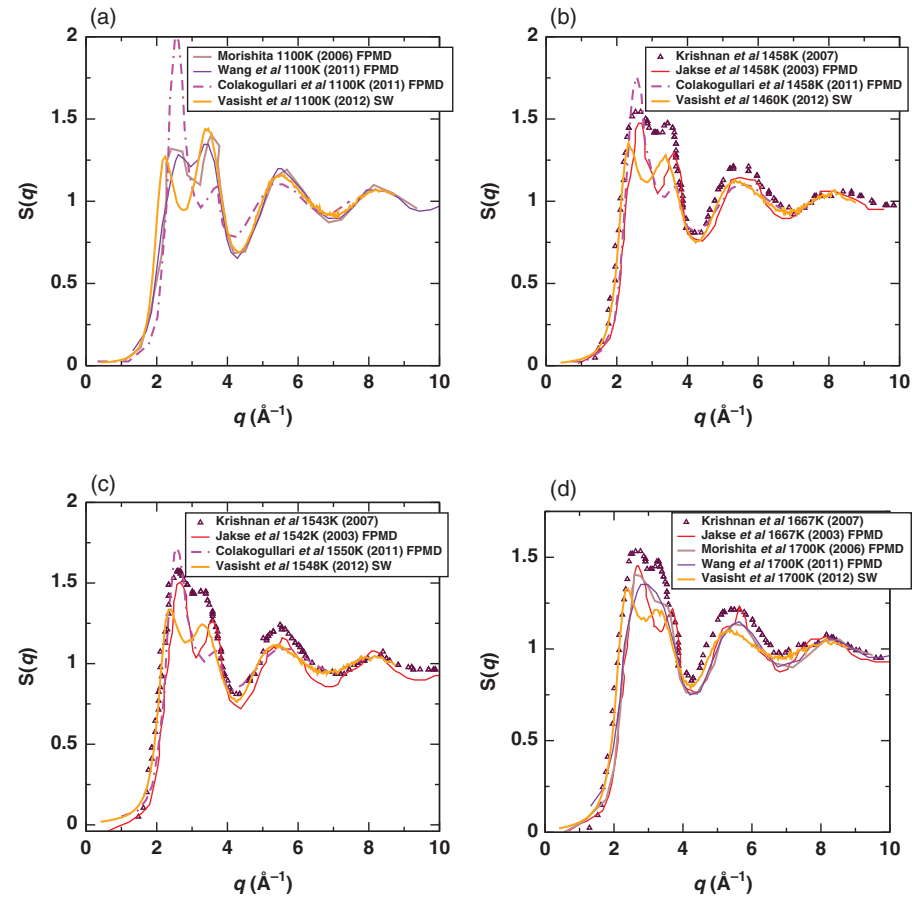
Figure 18.42. Comparison of the structure factor S(q) from different simulation works at four different temperatures, $T = 1100K$, $T \approx 1455K$, $T \approx 1550K$ and $T \approx 1700K$. We also show the recent experimental S(q) measurements for comparison purposes. [From Krishnan et al. [75], Jakse et al. [74], Morishita [45], Wang et al. [105] and Colakogullari et al. [106] with permission.]
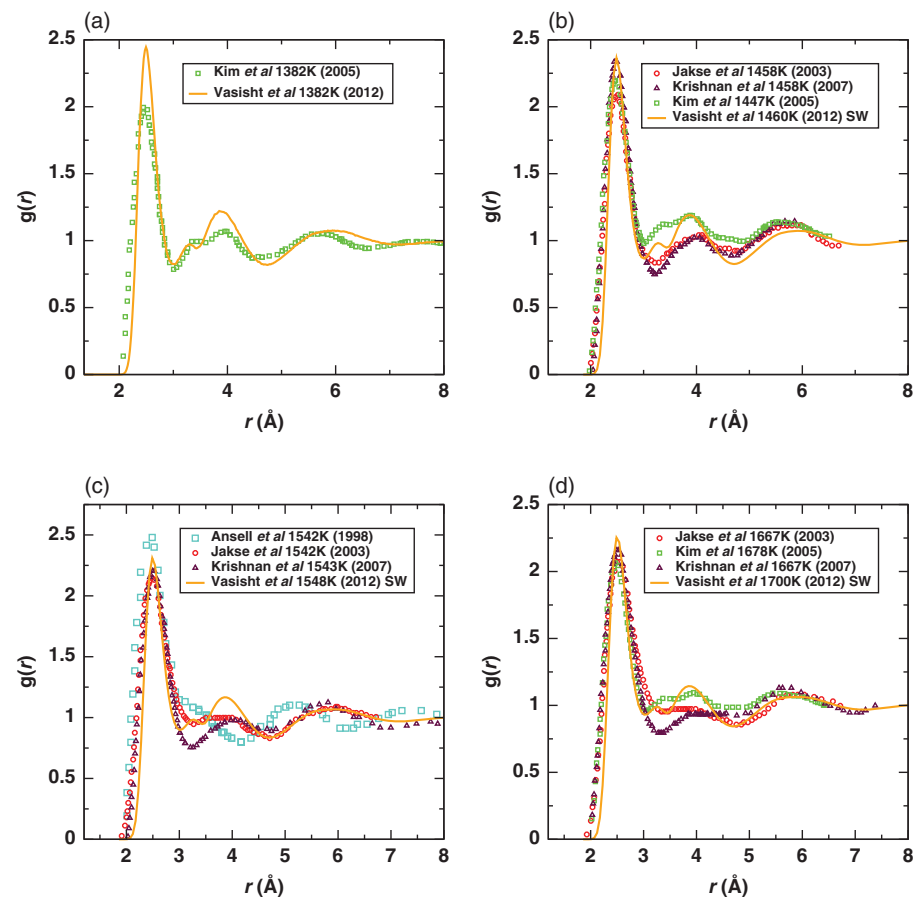
Figure 18.43. Comparison of the pair correlation function g(r) from NPT MD simulations using the SW potential and from experiments at four different temperatures, $T = 1382K$, $T \approx 1455K$, $T \approx 1550K$ and $T \approx 1770K$. [From Ansell et al. [73], Jakse et al. [74], Kim et al. [81], Krishnan et al. [75] with permission.]
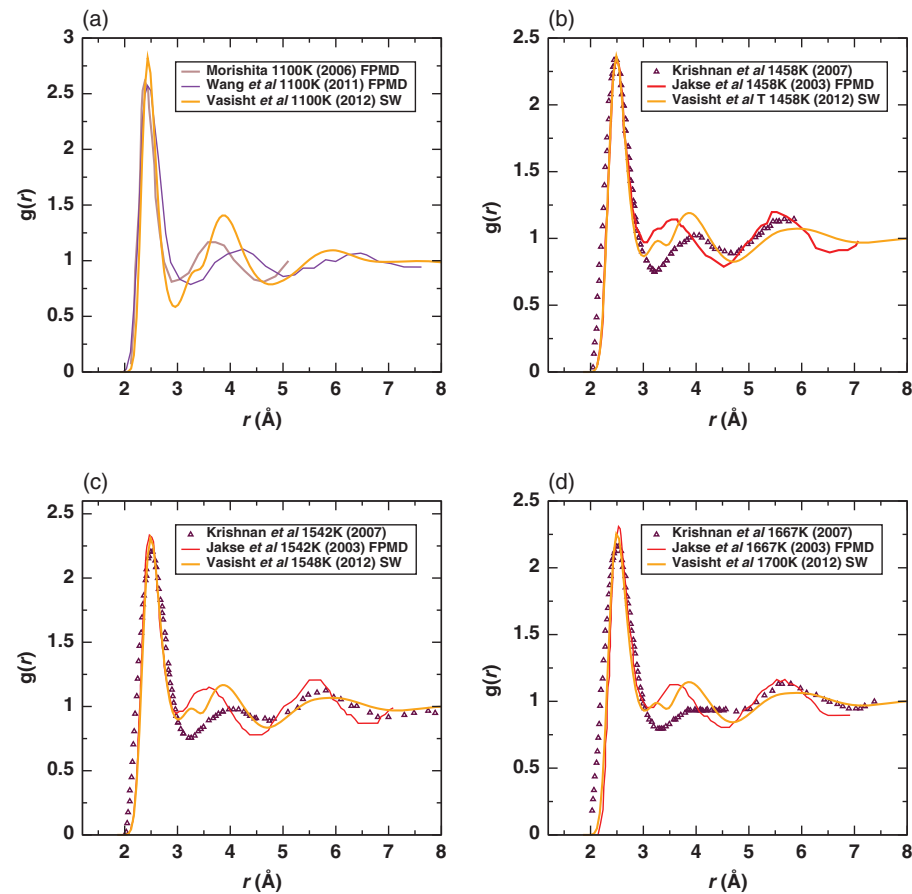
Figure 18.44. Comparison of the pair correlation function g(r) from different simulation works at four different temperatures, $T = 1100K$, $T \approx 1455K$, $T \approx 1550K$ and $T \approx 1700K$. We also show the recent experimental g(r) measurements for comparison purposes. [From Krishnan et al. [75], Jakse et al. [74], Morishita [45], Wang et al. [105] and Colakogullari et al. [106] with permission.]
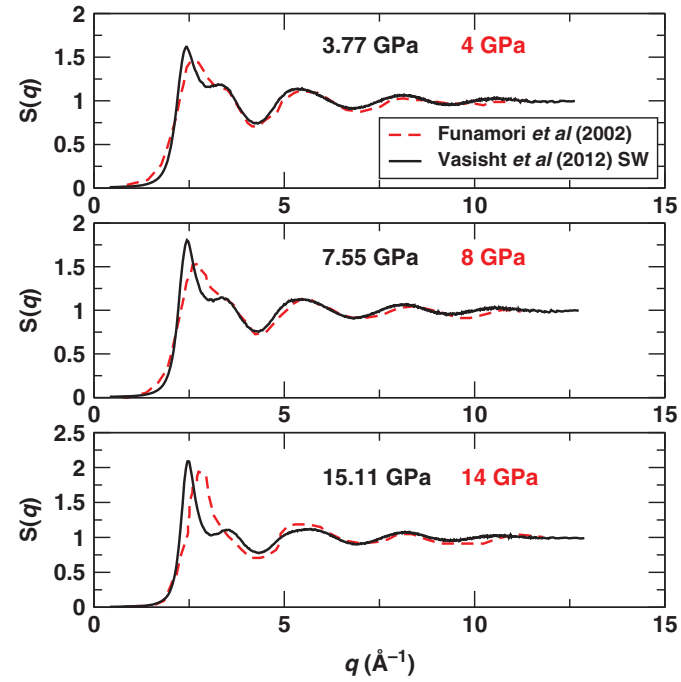
Figure 18.45. Comparison of the structure factor S(q) from NPT MD simulations using the SW potential with the experimental data at high pressure values for $T = 1737K$. [From Funamori et al. [107] with permission.]
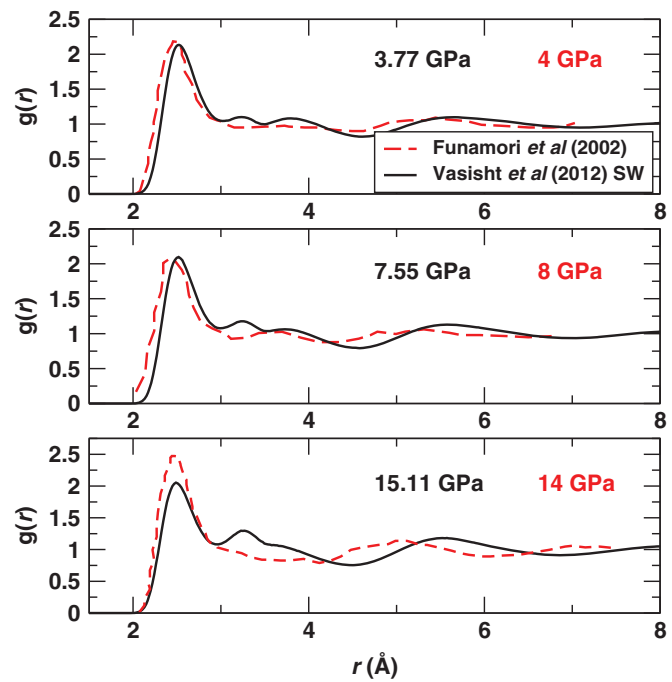
Figure 18.46. Comparison of the pair correlation function g(r) from NPT MD simulations using the SW potential with the experimental data at high pressure values for $T = 1737$K. [From Funamori et al. [107] with permission.]
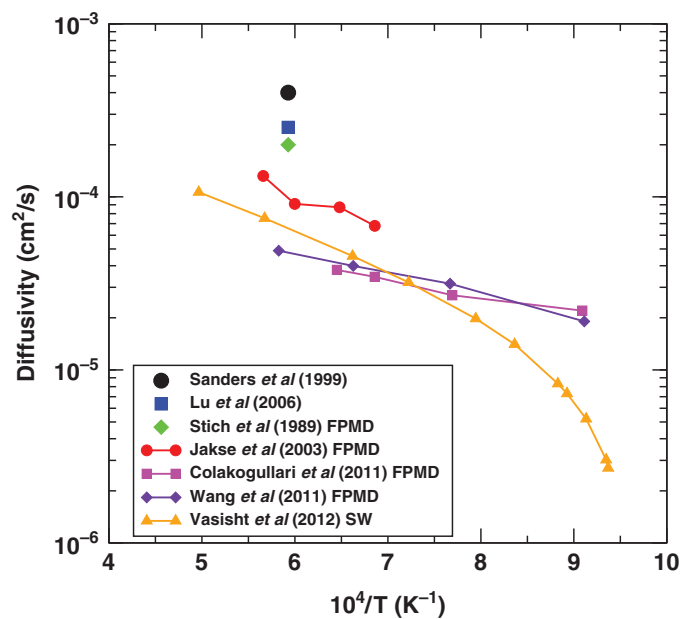
Figure 18.47. Compilation of Diffusivity against inverse temperature as reported by different experimental reports, first-principle MD (FPMD) simulations along with the simulation results using the SW potential. [From Stich et al. [44], Jakse et al. [74], Colakogullari et al. [106], Wang et al. [105], Sanders et al. [108], Lu et al. [109] with permission.]